Volume 14
Number 24
28 June 2022
Pages 8551-8888

Nanoscale

rsc.li/nanoscale

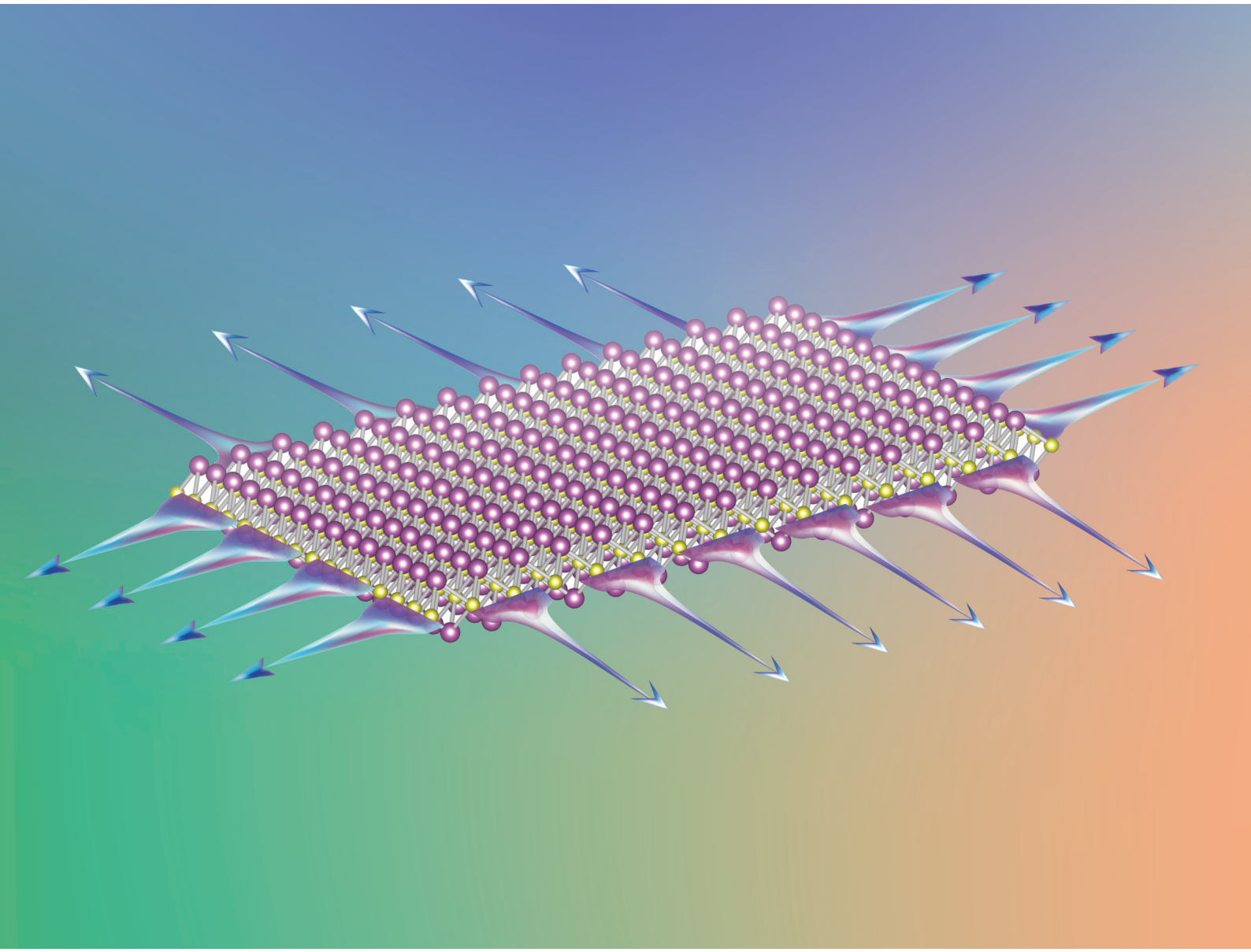

ISSN 2040-3372

ROYAL SOCIETY OF CHEMISTRY

PAPER
Zenner S. Pereira, Giovani M. Faccin and E. Z. da Silva
Strain-induced multigap superconductivity in electrene Mo_2N: a first principles study

NCNST

Nanoscale

ROYAL SOCIETY OF CHEMISTRY

PAPER

View Article Online
View Journal | View Issue

Cite this: *Nanoscale*, 2022, **14**, 8594

Strain-induced multigap superconductivity in electrene Mo_2N: a first principles study†

Zenner S. Pereira, *‡[a] Giovani M. Faccin ‡[b] and E. Z. da Silva *‡[c]

Received 20th January 2022,
Accepted 11th May 2022

DOI: 10.1039/d2nr00395c

rsc.li/nanoscale

Superconductivity in low dimensional materials and 2D electrides are topics of great interest with possible applications in next generation electronic devices. Using density functional theory (DFT) associated with Migdal-Eliashberg approach and maximally localized Wannier functions this study shows how biaxial strain affects superconductivity in a monolayer of Mo_2N. Results indicate that 2D Mo_2N presents strong electron–phonon coupling with large anisotropy in the superconducting energy gap. It is also proposed that, at low temperatures, a single layer of Mo_2N becomes an electride with localized electron gas pockets on the surface, resembling anions adsorbed on an atomic sheet. Calculations point to T_c = 24.7 K, a record high transition temperature for this class of material at ambient pressure. Furthermore, it is shown that when biaxial strain is applied to a superconducting Mo_2N monolayer, a new superconductivity gap starts at 2% strain and is enhanced by continuum strain, opening additional coupling channels.

1. Introduction

Recently, low dimensional materials have been used as a platform to study materials completely dominated by quantum effects. Superconductivity achieved by electron–phonon coupling (EPC) is one relevant property that some two-dimensional (2D) materials present.[1,2] When electrons are confined in 2D space, they present, in many cases, unexpected effects not found in three-dimensional (3D) materials. A classical example comes from 2D molybdenum disulfide (MoS_2), which is described as a graphene-like 2D transition metal dichalcogenide (TMDC).[3] In MoS_2, physical and chemical properties are very different depending on the number of layers and, while layered structure has an indirect bandgap, the MoS_2 monolayer is a direct bandgap semiconductor.[4] Experimental results demonstrate that superconductivity can be induced in a monolayer of MoS_2 just by proximity to a Pb(111) surface[5] or gated doping,[6,7] even though it is a semiconductor when in a free-standing form.

2D materials can also be electrides. Electrides are materials where the electron gas is spatially decoupled from the ions and confined in a well-defined region in the interstices.[8] In electrides, when electrons are quantum confined in pockets, they behave very similar to an anion localized in a site of the crystal.[9,10] The electron gas can also be spread in an isolated layer of electrons[11–13] or, for example, confined in regions resembling an hexagonal topology.[14] Some electrides may present high electrical conductivity or superconductivity,[14,15] low work functions, and anisotropic optical response and can have potential applications such as electron emitters, work as anode materials in batteries and other applications.[16–19] When an electride has just one monolayer it is called electrene.[20] A representative electrene is Ca_2N,[12,13] where electrons form an electron gas layer on the surface.

Another class of 2D materials are MXenes that are formed by a monolayer of carbon or nitrogen (X) sandwiched by two transition metal layers (M).[21] Motivated by recent synthesis of layered Mo_2N by transformation of MXene carbides into 2D MXene nitrides using ammoniation,[22] we studied superconductivity in an isolated single layer of this material. In this work, we propose that a single layer of Mo_2N is an electrene superconductor with a large anisotropic gap, this anisotropy being dependent on biaxial strain. Since 2D materials usually have extraordinary mechanical properties[23] and strain engineering may tune the electronic band structures of materials,[24,25] we also applied biaxial strain in an isolated single layer up to its dynamical stability limit. The strain effect on materials has emerged as a research field named straintronics to study novel electronic properties mainly in 2D materials. As an example, it was recently demonstrated that strain modulates a continuous bandgap and piezo-resistive effect in black phosphorus.[26]

[a]*Departamento de Ciência e Tecnologia, Universidade Federal Rural do Semi-Árido (UFERSA), CEP 59780-000, Campus Caraúbas, RN, Brazil. E-mail: zenner.silva@ufersa.edu.br*
[b]*Faculdade de Ciências Exatas e Tecnológicas, Universidade Federal da Grande Dourados – Unidade II, CP 533, 79804-970, Dourados, MS, Brazil. E-mail: giovanifaccin@ufgd.edu.br*
[c]*Institute of Physics "Gleb Wataghin", UNICAMP, CP 6165, 13083-859, Campinas, SP, Brazil. E-mail: zacarias@ifi.unicamp.br*

†Electronic supplementary information (ESI) available. See DOI: https://doi.org/10.1039/d2nr00395c

‡The authors contributed equally to this work.

In a previous large theoretical study, Bekaert *et al.*[27] explored superconductivity in all MXene monolayer compounds, including Mo_2N. The presented results are important, evidencing superconductivity in this material. However, the calculated T_c values presented in that work have been limited to the semiempirical McMillan and Allen-Dynes formulae[28,29] and have not considered the possible effects of superconductivity gap anisotropy. In 2D materials the anisotropy of the superconducting gap is, in general, more significant than in bulk materials. As a consequence, semiempirical formulations may not describe well T_c values when layered materials have large anisotropic gaps. Even if the EPC parameter is small ($\lambda < 1$), anisotropic effects may cause significant deviation from isotropic assumptions.[30,31] For instance, heavy electron doped graphene has a large anisotropic gap and $\lambda = 0.42$. The Allen-Dynes formula, considering repulsive Coulomb interaction, gives $T_c \approx 1.3$ K, while the solution of a fully anisotropic Migdal-Eliashberg (ME) equation gives $T_c = 13$ K.[32,33] Layered MgB_2 is also strongly affected by low dimensional effects and has three separate anisotropic superconductivity gaps enhanced by biaxial strain.[34] Therefore, there are many cases of low dimensional materials in which it is important to consider anisotropy in order to obtain reasonable superconductivity results.

Superconductivity in bulk phase Mo_2N was also demonstrated in several experimental papers, with T_c values ranging from 3.8 to 5.2 K depending on the phase of Mo_2N.[35–37] In contrast to recently synthesized layered Mo_2N, the bulk phase, in general, has structural vacancies necessary for the material's stability, leading to a hard computational simulation study. In this paper, simulations are limited to a single layer of Mo_2N.

2. Methodology

Two-dimensional Mo_2N is studied using density functional theory (DFT)[38,39] as implemented in the Quantum Espresso (QE) package.[40,41] To this end, Kohn–Sham equations were solved in the framework of the projector augmented-wave (PAW) method using pseudopotentials in the GGA approximation at the PBE level,[42,43] with the following projectors: $4s^2$, $4p^6$, $4d^5$ and 5s for Mo and $3s^2$ and $2p^3$ for N. The kinetic energy cutoff for wavefunctions was set to 70 Ry and a charge density cutoff of 380 Ry was chosen. Optimized periodic replicas are 18 Å apart when measured along the $\hat{z}$ direction. Phonon frequencies were analysed using density functional perturbation theory (DFPT).[44] Isotropic and anisotropic Migdal-Eliashberg (ME) equations were solved using the electron-phonon Wannier (EPW) module.[45–47] In the ME equation, the imaginary axis formulation is used to determine the superconducting gap and T_c, while the real axis is used to estimate spectral properties, such as quasiparticle density of states, which are calculated *via* analytic continuation of the solutions along the imaginary axis using Padé approximants.[48]

As a relative coarse mesh a $28 \times 28 \times 1$ k-grid and a $14 \times 14 \times 1$ grid for q-point evaluation with a Monkhorst–Pack mesh centered at the Γ point was used in the simulations. In order to obtain super dense discretization for the reciprocal space, Wannier functions were used to interpolate the band structure. We used finer interpolation grids of $100 \times 100 \times 1$ for both the k-mesh and q-mesh in this last step.

In the ME equation, the upper limit over frequency integration was 0.75 eV, which represents 10 times the maximum phonon frequency found in Mo_2N. The convergence threshold used for the iterative solution of imaginary-axis Eliashberg equations was 10^{-6}. The width of the Fermi surface window to take into account states in self-energy delta functions was 1.0 eV. EPC parameter results were tested for 10 different phonon smearing and two electron smearing values. Convergence of results for both isotropic and anisotropic solutions were also tested at 3% strain using a finer grid of $120 \times 120 \times 1$ leading essentially to the same results. The semiempirical Coulomb parameter μ^* was set to 0.13; this value is expected for a transition metal.[49]

It is also important to point out that DFT band structure calculation and Wannierization are in complete agreement with each other. The idea employed to get super dense grids necessary to the superconductivity calculation is to have a set of maximally localized Wannier functions obtaining very low spreads, leading to perfect fitted bands. Therefore, in the superconductivity calculations, the DFT band structure can be changed by the Wannier band structure having a reduced computational cost. For DFT and Wannier band structures see the figures related to methodology in the ESI.†

Interstitial and projected density of states (DOS, IDOS or PDOS) were calculated using the methodology implemented in ELK code, an all-electron full-potential linearised augmented-plane wave (LAPW) package.[50] The electronic k-mesh was $60 \times 60 \times 1$ and the muffin-tin radius was 1.25 Å for molybdenum species and 0.86 Å for nitrogen. We set very high quality parameters in order to change default parameters to ensure excellent convergence.

3. Results

The relaxed structure of layered Mo_2N gives structural parameters $a = b = 2.907$ Å and $c = 15.04$ Å. This structure is well represented by the trigonal space group number 166 and lattice parameters are in accordance with recent experimental work.[22] Simulated structural parameters for the isolated single layer reduces spatial group symmetry to number 164 and presents $a = b = 2.803$ Å, that is slightly different from a layered material. These values are very similar to those of Bekaert *et al.*[27] The results associated with the electrene state for the isolated monolayer are shown in Fig. 1. We used electron localization function (ELF) to identify electron pockets. The ELF value equal to 0.5 represents an electron gas; values above 0.5 indicate localized electrons and below 0.5 indicate delocalized electrons.[51] In Fig. 1a–c, the interstitial sites at the surface are filled by electron pockets with ELF values up to 0.6. A volumetric section taking the ELF isovalue equal to 0.5 is shown in

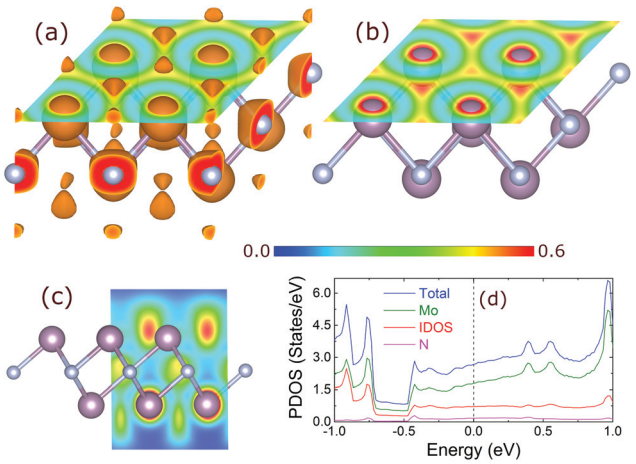

Fig. 1 Structure, ELF and DOS for Mo_2N. (a–c) A structural model (2 × 2 × 1 unit cell) of a single layer of Mo_2N colored by ELF maps, whose values follow the schematic color ranges from 0.0 (blue) to 0.6 (red). (a) A volumetric section taking the ELF isovalue equal to 0.5 (orange color). In addition, a transparent lattice plane, also following the schematic color map explained before, is also shown on top of the surface. (b) The same image shown in (a), except for removing the isovolumetric section. (c) A vertical section plane showing the electron pockets in another perspective. (d) DOS, PDOS on atoms and IDOS for a relaxed single layer.

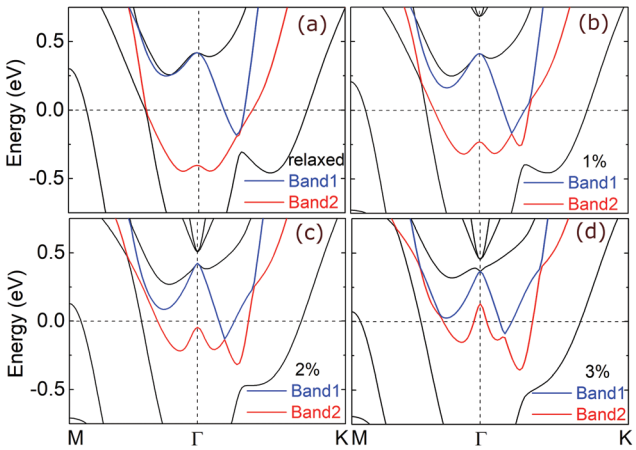

Fig. 2 Mo_2N monolayer band structures of relaxed (0%) (a) and monolayer stressed by 1% (b), 2% (c) and 3% (d) of biaxial strain, respectively. Two featured bands are colored (labeled) in blue (band1) and red (band2). The figures show band changes depending on strain.

1a (0.5 value is coded as orange color), it shows electron pockets at the interstitial sites and it is also observed that ELF values between electron pockets and Mo atoms are far below 0.5. These interstitial electron pockets are also called interstitial quasiatoms (ISQs).[52] In addition, a lattice plane section colored by ELF map is also shown in Fig. 1a and b, showing localized electron pockets. Fig. 1c shows a transverse plane through the pockets, also colored by the ELF map. The total ISQ charge is $5.3e^-$ per unit cell. This localized charge density represented by pockets generates a significant effect on the surface, similar to having a small anionic species adsorbed on it. In addition, Fig. 1d presents the total, interstitial and projected density of states per unit cell. At the Fermi level, the Mo species is responsible for 67% of the total DOS, while IDOS represents 27% and nitrogen atoms contribute 6%. Therefore, although IDOS is not the largest one, its contribution is very important and simulates an electronic effect comparable to having a small anionic species on the surface. These findings characterize an electride state where the electron gas is confined in a specific region of the crystal and spatially isolated from the ions.

The band structures of relaxed and biaxially strained monolayers were studied up to the limit of their dynamical stability, which was found to be 5% strain. When strain reaches 6%, the system becomes unstable, a fact that can be verified through imaginary frequencies in acoustic modes. Fig. 2a–d show DFT band structures for relaxed and stressed monolayers; it presents how the band structure near the Fermi level is affected by strains of 1%, 2% and 3%. Bands shown along the M–Γ–K paths are the ones particularly relevant for changes in superconducting properties presented in this study. Fig. 2 indicates continuous transformation of bands, mainly around the Γ point, caused by strain, pushing one valence band (colored in red) into the Fermi level. On the other hand, one conduction band moves downward into the Fermi level (colored in blue). At 2% strain, the modified valence bands are very close to the Fermi level, just 47 meV bellow the Γ point. At 3%, band2 creates a new crossing around the Γ point. Changes continue due to strain and at 4% (not shown) bands create one more new crossing at the Fermi level along the Γ–M line, a consequence of the conduction band's (band1) new crossing. Band transformations have significant impact on the electronic properties of this material; although an electride state is kept, superconductivity properties undergo important changes. The proximal effect of bands towards the Fermi level, leading to additional crossovers, triggers new contributions to EPC. As a consequence, a new superconductivity gap starts at 2% strain, whose details will be further discussed in the final part of this article. Since projected bands on angular momentum character are not defined at interstitial sites, we are limited to calculating them only at atoms. By doing so, we find that all bands near the Fermi level have mainly d-character coming from molybdenum. The complete set of band structures for monolayer Mo_2N, with and without the spin orbit coupling (SOC) interaction, is provided in the ESI.†

Mo_2N presents interesting superconducting properties. First, isotropic spectral function analysis shows that, for the unstrained case, the main contribution to EPC comes from acoustic phonon modes along the M–Γ–K (72.8%) line with a smaller contribution from optical modes (27.2%), mainly around the Γ point. Phonon density of states and spectral function demonstrate that almost all phonon contribution for the EPC comes from molybdenum, mostly caused by acoustic phonons. Also, an important part is obtained from optical traverse modes around 23 meV (5.6 THz) near the Γ point, which represents a transverse breathing mode along the z direction.

However, for the strained monolayer, the picture changes; as shown in Fig. 3 the EPC parameter related to acoustic phonons is significantly modified by strain effects. It is strongly reduced up to 3% strain and, above this value, increases again. On the other hand, the EPC parameter contribution related to optical modes is not affected up to 2% strain and then it is slightly increased from 3% to 5% strain. At 3% strain, acoustic phonon contribution decreases and represents only 53.5% of the EPC parameter, that is significantly smaller than the relaxed case. Its optical modes contribute as a source of almost half the superconductivity at 3% strain. In this case, an enhanced EPC parameter related to optical modes is connected with the band structure, as shown in Fig. 2a–d. New band crossing, caused by strain, leads to a relevant and novel EPC contribution near the Γ point, as demonstrated by projected spectral function in optical and acoustic modes. Although the EPC parameter related to optical modes increases, the total EPC parameter is still strongly affected by acoustic modes. Therefore, under strain, acoustic phonons decrease their absolute contribution to the EPC parameter, in contrast, optical phonon modes increase their contribution when strain achieves 3% and above. Summing up, the overall scenario for the total EPC parameter and T_c values is as follows: λ and T_c decreases up to 2% strain and, above this value, increases again by the sum of different contributions from acoustic and optical modes, as a consequence of a new band structure scenario and modified phonon curve dispersion. See the ESI† for a set of figures related to EPC.

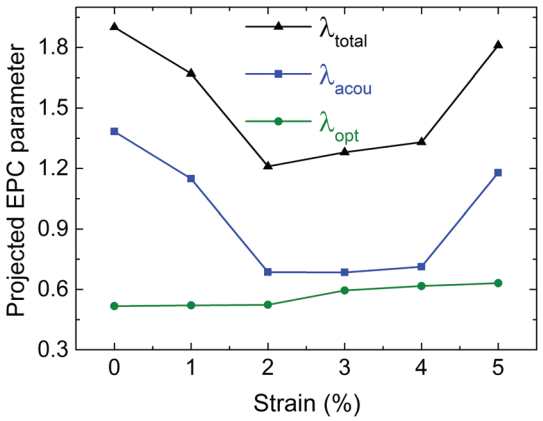

Fig. 3 Total EPC parameter evaluated as a function of strain, splits into the acoustic EPC parameter (blue line) and optical contribution (green line).

Fig. 4a and b show isotropic and anisotropic energy distributions of the superconducting gap as a function of temperature for relaxed and strained monolayers, respectively. It can be seen that the isotropic ME equation underestimates the T_c value and superconducting gap when compared to the fully

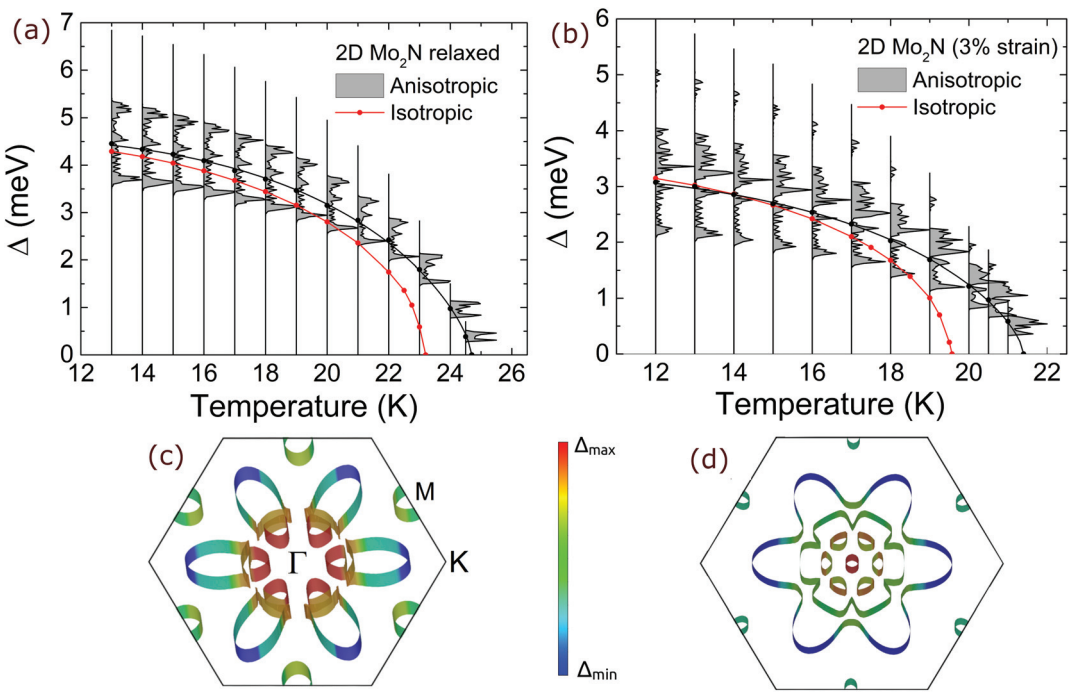

Fig. 4 Computed isotropic gap (red line) and energy distribution of anisotropic superconducting gap Δ, evaluated as a function of temperature for (a) unstrained 2D Mo_2N and (b) 3% strained materials. In order to estimate T_c for the anisotropic case, a solid black line is taken in the center of the gap and this line is extrapolated for $\Delta = 0$ *via* exponential approximation $\Delta = \Delta_0[1 - (T/T_c)^p]^{1/q}$, with Δ_0, p, q and T_c being adjustable parameters. (c) and (d) The Fermi surface colored by the value of the anisotropic gap (Δ_k) at unstrained and strained cases at 15 K, respectively. Blue and red on the Fermi sheet represent the minimum and maximum values of the gap, respectively. Only parts of the Fermi sheets that have $\Delta_k > 0$ are shown. Parts of the Fermi sheets in which $\Delta_k = 0$ are make invisible. The Coulomb parameter used was $\mu^* = 0.13$.

anisotropic ME equation. An important effect is observed in Fig. 4b for 3% strain. In the unstressed single layer, we find an anisotropic gap (Fig. 4a); however, at 3% strain, the results show one more isolated and small superconducting gap, slightly anisotropic, with energy above the first one, around 5 meV at 12 K. This new gap is completely related to the band structure and Fermi surface (FS) at the first Brillouin zone, which is colored by the binding energy of Cooper pairs (Δ_k) in Fig. 4c and d for relaxed and strained cases, respectively. First, at 3% strain, a decrease is observed in the area of the FS compared to 0% strain. This is linked to a smaller λ parameter found for the strained monolayer compared to a relaxed case. Second, a new and small circular sheet with stronger values of Δ_k is found around the Γ point. The Fermi surface is related to four bands crossing the Fermi level. Although there are clearly five sheets shown in Fig. 4d, one FS has two branches (sheets), which are associated with the band structure (band2) shown in Fig. 2d. This new circular sheet found close to the Γ point leads to several consequences for superconductivity properties, one of them being the appearance of a new superconducting gap leading to a multigap problem as shown in Fig. 4b, as a result of applied strain. The Δ_k distributions are spread on the four Fermi surfaces with four or five sheets depending on strain. Since the Δ_k distribution is spread on the Fermi surface, it is expected that the EPC parameter has also an anisotropic distribution λ_k. For instance, considering the electronic states with momentum k on the FS, in the relaxed case, we find $1.10 < \lambda_k < 3.3$, and for 3% strain, we find $0.4 < \lambda_k < 3.5$, which corroborates the important anisotropic effect in the problem. See the ESI† for figures related to the anisotropic gap for different strain values.

Fig. 5 shows the normalized quasiparticle density of states at 2.5 K for relaxed and 3% strained structures obtained using Padé approximants,[48] and superconducting gaps are shown. For the relaxed monolayer, we observed a peak in the SC DOS at 6 meV and also important curlings in the SC DOS around 5 meV (indicated by blue arrows), which is related to the central peak of the Δ_k distribution shown in Fig. 4a. It appears that there are two superimposed gaps, a small one at around 5 meV and the main one at 6 meV. This indicates the effect of gap energy spread (anisotropy) on the FS sheets and also corroborates that there are Δ_k distributions overlapped on the FS in accordance with Fig. 4. The strained monolayer shows a main peak in the SC DOS around 4.2 meV at the same temperature. The overall effect of this slightly anisotropic gap related to the circular sheet around the Γ point can also be observed in the superconducting DOS (SC DOS). Red arrows indicate a small peak (curling) near 5.5 meV at 3% strain which corresponds to values for Δ_k at 2.5 K linked to the new circular FS sheet caused by strain as discussed before. A small effect in the superconducting DOS is expected since the energy distribution of the Cooper pairs in the new FS sheet is much smaller and shorter than the total effect coming from other FS sheets with lower gap energy.

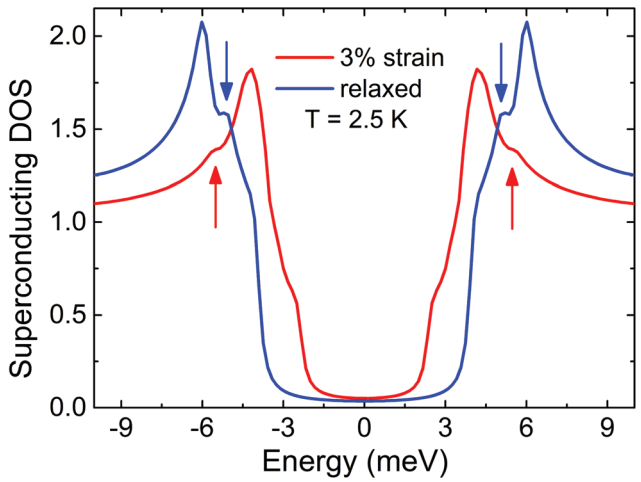

Fig. 5 Normalized quasiparticle density of states at 2.5 K for the relaxed Mo_2N monolayer (blue) and 3% strain (red).

As a final point, in order to qualitatively understand what is the electron pocket contribution to the superconductivity, we also simulated the band structure for an hydrogenated Mo_2N monolayer. The hydrogen atoms are placed on the electron pockets in both sides of the layer and this new structure is fully relaxed. The proposal of this computational procedure is to decide which bands correspond to the electron pockets by comparison between the band structure with and without hydrogen. As a result, the pockets remained strongly bounded to hydrogen atoms and band lines associated with the pockets were pushed far away from the Fermi level, as shown in Fig. S8 provided in the ESI.† We conclude that the band line that crosses the Fermi level (band4, Fig. S8 in the ESI†) near the M point corresponds to the conduction band of the pockets for the pure single layer (without hydrogen). It is also represented by the small circular Fermi surface at the M point shown in Fig. 4c and d, and it is also related to the small density of states at the Fermi level that comes from interstitial sites (27%). It is important to note that, the contribution for the superconductivity coming from the Fermi surface only around the M point is very small, therefore, we conclude that the electron pockets represent only a small but important part of the electron–phonon interaction. Thus, superconductivity mainly comes from the 4d electrons of molybdenum.

4. Conclusions

In conclusion, using first principles calculations, we suggest that the new findings of the present work are: (i) the Mo_2N monolayer is an electride with electron pockets on its surface and at sufficiently low temperatures is a strong interaction superconductor. (ii) If biaxially strained, band structure engineering leads to important changes in the FS, as well as in phonon dispersions. As a consequence, superconducting properties are significantly modified, mainly with respect to the superconducting gap. (iii) Solution of the anisotropic ME equation can not be neglected in order to understand how

superconductivity occurs in a Mo_2N monolayer. (iv) For the pure electride monolayer without gated or chemical doping T_c values range from 19.3 K to 24.8 K as a function of strain, the latter being a record high value for this class of material at ambient pressure, to our knowledge. Finally, the possibility of controlling T_c by strain manipulation is very interesting and we believe that the results that go beyond isotropic approximations in order to include anisotropic effects are important and could be useful to foment experimental studies and enable further investigation in MXenes.

Author contributions

These authors contributed equally to this work.

Conflicts of interest

There are no conflicts to declare.

Acknowledgements

Simulations were performed at CCJDR-Unicamp, Cenapad-SP – Centro Nacional de Processamento de Alto Desempenho em São Paulo. We acknowledge support from FAPESP (2013/07296-2, 2016/23891-6 and 2017/26105-4) and CNPq. Cover Art by Desayuno.

References

1 Y. Saito, T. Nojima and Y. Iwasa, *Nat. Rev. Mater.*, 2016, **2**, 16094.
2 G. Profeta, M. Calandra and F. Mauri, *Nat. Phys.*, 2012, **8**, 131–134.
3 S. Manzeli, D. Ovchinnikov, D. Pasquier, O. V. Yazyev and A. Kis, *Nat. Rev. Mater.*, 2017, **2**, 17033.
4 E. S. Kadantsev and P. Hawrylak, *Solid State Commun.*, 2012, **152**, 909–913.
5 D. J. Trainer, B. Wang, F. Bobba, N. Samuelson, X. Xi, J. Zasadzinski, J. Nieminen, A. Bansil and M. Iavarone, *ACS Nano*, 2020, **14**, 2718–2728.
6 J. T. Ye, Y. J. Zhang, R. Akashi, M. S. Bahramy, R. Arita and Y. Iwasa, *Science*, 2012, **338**, 1193–1196.
7 K. Taniguchi, A. Matsumoto, H. Shimotani and H. Takagi, *Appl. Phys. Lett.*, 2012, **101**, 042603.
8 X. Zhang and G. Yang, *J. Phys. Chem. Lett.*, 2020, **11**, 3841–3852.
9 J. L. Dye, *Acc. Chem. Res.*, 2009, **42**, 1564–1572.
10 S. Matsuishi, Y. Toda, M. Miyakawa, K. Hayashi, T. Kamiya, M. Hirano, I. Tanaka and H. Hosono, *Science*, 2003, **301**, 626–629.
11 K. Lee, S. W. Kim, Y. Toda, S. Matsuishi and H. Hosono, *Nature*, 2013, **494**, 336–340.
12 S. Zhao, Z. Li and J. Yang, *J. Am. Chem. Soc.*, 2014, **136**, 13313–13318.
13 D. L. Druffel, K. L. Kuntz, A. H. Woomer, F. M. Alcorn, J. Hu, C. L. Donley and S. C. Warren, *J. Am. Chem. Soc.*, 2016, **138**, 16089–16094.
14 Z. S. Pereira, G. M. Faccin and E. Z. da Silva, *J. Phys. Chem. C*, 2021, **125**, 8899–8906.
15 Z. Zhao, S. Zhang, T. Yu, H. Xu, A. Bergara and G. Yang, *Phys. Rev. Lett.*, 2019, **122**, 097002.
16 Y. Toda, S. W. Kim, K. Hayashi, M. Hirano, T. Kamiya, H. Hosono, T. Haraguchi and H. Yasuda, *Appl. Phys. Lett.*, 2005, **87**, 254103.
17 J. Hu, B. Xu, S. A. Yang, S. Guan, C. Ouyang and Y. Yao, *ACS Appl. Mater. Interfaces*, 2015, **7**, 24016–24022.
18 J. Hou, K. Tu and Z. Chen, *J. Phys. Chem. C*, 2016, **120**, 18473–18478.
19 C. Liu, S. A. Nikolaev, W. Ren and L. A. Burton, *J. Mater. Chem. C*, 2020, **8**, 10551–10567.
20 D. L. Druffel, A. H. Woomer, K. L. Kuntz, J. T. Pawlik and S. C. Warren, *J. Mater. Chem. C*, 2017, **5**, 11196–11213.
21 K. A. Papadopoulou, A. Chroneos, D. Parfitt and S.-R. G. Christopoulos, *J. Appl. Phys.*, 2020, **128**, 170902.
22 P. Urbankowski, B. Anasori, K. Hantanasirisakul, L. Yang, L. Zhang, B. Haines, S. J. May, S. J. L. Billinge and Y. Gogotsi, *Nanoscale*, 2017, **9**, 17722–17730.
23 S. Deng, A. V. Sumant and V. Berry, *Nano Today*, 2018, **22**, 14–35.
24 F. Miao, S.-J. Liang and B. Cheng, *npj Quantum Mater.*, 2021, **6**, 59.
25 A. Chaves, J. G. Azadani, H. Alsalman, D. R. da Costa, R. Frisenda, A. J. Chaves, S. H. Song, Y. D. Kim, D. He, J. Zhou, A. Castellanos-Gomez, F. M. Peeters, Z. Liu, C. L. Hinkle, S.-H. Oh, P. D. Ye, S. J. Koester, Y. H. Lee, P. Avouris, X. Wang and T. Low, *npj 2D Mater. Appl.*, 2020, **4**, 29.
26 Z. Zhang, L. Li, J. Horng, N. Z. Wang, F. Yang, Y. Yu, Y. Zhang, G. Chen, K. Watanabe, T. Taniguchi, X. H. Chen, F. Wang and Y. Zhang, *Nano Lett.*, 2017, **17**, 6097–6103.
27 J. Bekaert, C. Sevik and M. V. Milošević, *Nanoscale*, 2020, **12**, 17354–17361.
28 W. L. McMillan, *Phys. Rev.*, 1968, **167**, 331–344.
29 P. B. Allen and R. C. Dynes, *Phys. Rev. B: Solid State*, 1975, **12**, 905–922.
30 C. Heil, S. Poncé, H. Lambert, M. Schlipf, E. R. Margine and F. Giustino, *Phys. Rev. Lett.*, 2017, **119**, 087003.
31 C.-S. Lian, C. Si and W. Duan, *Nano Lett.*, 2021, **21**, 709–715.
32 E. R. Margine and F. Giustino, *Phys. Rev. B: Condens. Matter Mater. Phys.*, 2014, **90**, 014518.
33 G. Eliashberg, *Sov. Phys. JETP-USSR*, 1960, **11**, 697–702.
34 J. Bekaert, A. Aperis, B. Partoens, P. M. Oppeneer and M. V. Milošević, *Phys. Rev. B*, 2017, **96**, 094510.
35 C. Wang, Y. H. Wang, X. Wu, X. K. Li and J. W. Luo, *Mater. Lett.*, 2021, **287**, 129292.
36 K. Inumaru, K. Baba and S. Yamanaka, *Chem. Mater.*, 2005, **17**, 5935–5940.

37 C. L. Bull, T. Kawashima, P. F. McMillan, D. Machon, O. Shebanova, D. Daisenberger, E. Soignard, E. Takayama-Muromachi and L. C. Chapon, *J. Solid State Chem.*, 2006, **179**, 1762–1767.
38 P. Hohenberg and W. Kohn, *Phys. Rev.*, 1964, **136**, B864–B871.
39 W. Kohn and L. J. Sham, *Phys. Rev.*, 1965, **140**, A1133–A1138.
40 P. Giannozzi, S. Baroni, N. Bonini, M. Calandra, R. Car, C. Cavazzoni, D. Ceresoli, G. L. Chiarotti, M. Cococcioni, I. Dabo, A. D. Corso, S. de Gironcoli, S. Fabris, G. Fratesi, R. Gebauer, U. Gerstmann, C. Gougoussis, A. Kokalj, M. Lazzeri, L. Martin-Samos, N. Marzari, F. Mauri, R. Mazzarello, S. Paolini, A. Pasquarello, L. Paulatto, C. Sbraccia, S. Scandolo, G. Sclauzero, A. P. Seitsonen, A. Smogunov, P. Umari and R. M. Wentzcovitch, *J. Phys.: Condens. Matter*, 2009, **21**, 395502.
41 P. Giannozzi, O. Andreussi, T. Brumme, O. Bunau, M. B. Nardelli, M. Calandra, R. Car, C. Cavazzoni, D. Ceresoli, M. Cococcioni, N. Colonna, I. Carnimeo, A. D. Corso, S. de Gironcoli, P. Delugas, R. A. DiStasio, A. Ferretti, A. Floris, G. Fratesi, G. Fugallo, R. Gebauer, U. Gerstmann, F. Giustino, T. Gorni, J. Jia, M. Kawamura, H.-Y. Ko, A. Kokalj, E. Küçükbenli, M. Lazzeri, M. Marsili, N. Marzari, F. Mauri, N. L. Nguyen, H.-V. Nguyen, A. O. de-la Roza, L. Paulatto, S. Poncé, D. Rocca, R. Sabatini, B. Santra, M. Schlipf, A. P. Seitsonen, A. Smogunov, I. Timrov, T. Thonhauser, P. Umari, N. Vast, X. Wu and S. Baroni, *J. Phys.: Condens. Matter*, 2017, **29**, 465901.
42 P. E. Blöchl, *Phys. Rev. B: Condens. Matter Mater. Phys.*, 1994, **50**, 17953–17979.
43 J. P. Perdew, K. Burke and M. Ernzerhof, *Phys. Rev. Lett.*, 1996, **77**, 3865–3868.
44 S. Baroni, S. de Gironcoli, A. Dal Corso and P. Giannozzi, *Rev. Mod. Phys.*, 2001, **73**, 515–562.
45 F. Giustino, M. L. Cohen and S. G. Louie, *Phys. Rev. B: Condens. Matter Mater. Phys.*, 2007, **76**, 165108.
46 S. Poncé, E. Margine, C. Verdi and F. Giustino, *Comput. Phys. Commun.*, 2016, **209**, 116–133.
47 E. R. Margine and F. Giustino, *Phys. Rev. B: Condens. Matter Mater. Phys.*, 2013, **87**, 024505.
48 H. J. Vidberg and J. W. Serene, *J. Low Temp. Phys.*, 1977, **29**, 179–192.
49 G. Grimvall, *Phys. Scr.*, 1976, **14**, 63–78.
50 T. Müller, S. Sharma, E. K. U. Gross and J. K. Dewhurst, *Phys. Rev. Lett.*, 2020, **125**, 256402.
51 A. D. Becke and K. E. Edgecombe, *J. Chem. Phys.*, 1990, **92**, 5397–5403.
52 M.-s. Miao and R. Hoffmann, *J. Am. Chem. Soc.*, 2015, **137**, 3631–3637.

